Research Article

Actively Learned Optimal Sustainable Operation of Plasma-Catalyzed Methane Bireforming on $La_{0.7}Ce_{0.3}NiO_3$ Perovskite Catalyst

Diego Alexander Gonzalez-Casamachin,[||] Tian Qin,[||] Wei-Min Huang,* Srinivas Rangarajan,* Lihua Zhang, and Jonas Baltrusaitis*

Cite This: ACS Sustainable Chem. Eng. 2024, 12, 610−622

Read Online

ACCESS | Metrics & More | Article Recommendations | Supporting Information

ABSTRACT: Plasma-catalytic bireforming of methane was studied and actively optimized using a $La_{0.7}Ce_{0.3}NiO_3$ perovskite catalyst via experimentation in tandem with response surface modeling. Plasma power, inlet flow rate, temperature, CO_2/CH_4 ratio, and steam concentration were tuned to maximize a variety of process- and sustainability-based metrics. Analysis of the optimal conditions (with respect to different metrics) with and without the catalyst reveals that dry reforming is driven largely via noncatalytic reactions, while steam reforming and water gas shift reactions require the catalyst. The experimental outcome demonstrated that under optimum reaction conditions using the $La_{0.7}Ce_{0.3}NiO_3$ catalyst it is possible to minimize global warming potential (GWP), in terms of inferred CO_2 footprint normalized to hydrogen throughput, resulting in maximizing hydrogen yield through steam reforming (and water gas shift reactions) at an SEI of ≈12 eV/ molecule. Furthermore, the highest CH_4 conversion reached was 87% while the catalyst showed good activity stability in DBD plasma experiments. The actively learned iterative optimization procedure developed in this work allows for a direct juxtaposition of thermal (heat needed to make steam and heat the plasma reactor) and electrical (power requirement for plasma generation) carbon footprints in a highly nonlinear multivariate process. Furthermore, the corresponding GWP was calculated using a conventional electricity mix, wind electricity, and solar electricity, allowing a direct sustainability assessment in catalyst-assisted plasma conversion of carbonaceous feedstock to H_2 and CO.

KEYWORDS: plasma, perovskite, bireforming, hydrogen, sustainability indicator, green electricity
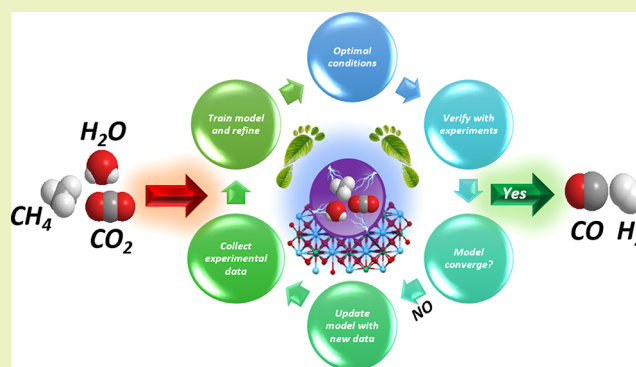
INTRODUCTION

Electrification of the chemical industry is needed to significantly decrease greenhouse gas (GHG) emissions from the current emission-intensive production technologies.[1] The production of ammonia and methanol, in particular, consumes large amounts of hydrogen (H_2) and syngas (CO+H_2), respectively. While hydrogen is an abundant element in many natural substances, fossil fuel reforming remains the predominant source of hydrogen supply in industry due to the combination of the highest energy efficiency and lowest price per kg H_2 produced.[2] To achieve this high efficiency, steam methane reforming (SMR) is usually carried at high temperatures to overcome not only kinetic but also thermodynamic limitations.[3] As a result, the SMR process possesses a very high carbon footprint with an estimated 9.35 kg of CO_2 equivalent/ kg H_2.[4] While the carbon footprint of processed methane is carried through the production process into the resulting products, such as methanol, sustaining temperatures in excess of 800 °C are achieved by burning fuel gas, which is often fuel

methane itself. This results in about 36% of exergy destroyed in the reformer and significant CO_2 emission.[5] Several methods have been proposed to alleviate the environmental and energy problems associated with reformer combustors to generate H_2 or syngas. The first development involves using electrical (ohmic) heating to maintain conventional SMR process temperatures[6−8] with added benefits of quick start-up, no thermal gradient, and well-controlled reaction extent. The second approach tackles the fundamental need to operate reforming reactions at high temperatures[9] by providing nonthermal molecular excitation to perform not only SMR[10] but also dry methane reforming (DMR)[11] and bireforming,
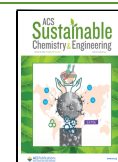
BRM (a combination of SMR and DMR),[12] at near room temperature. Nonthermal plasma (NTP), particularly dielectric barrier discharge (DBD) technology, offers a promising solution. NTP can break down CO_2 and CH_4 at room temperature, addressing the issues related to high-temperature operations in conventional methods. DBD reactors, known for their simplicity and mild conditions, show potential for decarbonizing reforming processes.[13,14]

For instance, Goujard et al. conducted research focused on generating syngas from biogas, composed of CO_2 and CH_4, using $LaNiO_3$ perovskite and nonthermal plasma under mild conditions. Their findings demonstrate that utilizing perovskites alongside discharge plasma aids in enhancing the activation of carbon dioxide. Additionally, the metallic nickel components function as radical traps, while the La_2O_3's basic properties, favoring CO_2 activation, result in heightened CO selectivity when combined with the catalyst and discharge plasma.[15]

In plasma-assisted processes, combining plasma reforming with catalysts greatly enhances CH_4 conversion and product selectivity.[16] However, a major challenge is the carbon-rich syngas formed from CO_2 and CH_4, leading to soot deposition on catalysts.[17] This issue can cause catalyst deactivation and reduced yields, hindering large-scale implementation. Two approaches have been explored to maintain stable catalysts during DMR. First, steam was introduced during the DBD plasma-assisted CO_2 and CH_4 reforming to increase the conversion of the reactants while reducing coke formation when compared to DMR.[12] This steam-facilitated reforming process is often referred to as bireforming and also has the benefit of yielding a higher H_2:CO ratio needed for downstream chemical production.[18] Second, perovskite-based catalysts have been utilized with cerium as a promoter. Liu et al. found that the La–Ce–Ni oxide catalyst exhibited promising activity in the steam reforming of ethanol at 600 °C under atmospheric pressure. This was attributed to the doping of La^{3+} into the CeO_2 lattice, resulting in the generation of more oxygen vacancies.[19]

The interaction of plasma and catalyst and the interplay of surface reactions and gas phase excitations (and reactions) are not yet fully understood.[20,21] The operating parameters of a plasma reactor, viz., plasma power, temperature, residence time, and feed composition, are nonlinearly related to reaction rates and product yield, and identifying the optimal conditions to maximize any chosen metric of interest is a matter of multivariate optimization. Identifying these optimal points via experimentation alone, although theoretically possible, is expensive. Consequentially, rigorously identifying optimal conditions requires the development and employment of a nonlinear model of the reaction system in tandem with experiments. In recent years, the response surface methodology (RSM), a statistical technique to learn a surrogate model from carefully designed experiments and the subsequent application of the ensuing model to identify optimal conditions, has gained traction to guide experiments.[22] Examples of RSM in optimizing catalytic systems include DBD plasma DMR,[23−25] ammonia synthesis,[26] nitric oxide reduction,[27] and ethanol reforming.[9] In these applications, a typical optimization is "static"; i.e., the models are trained once and then employed in optimization. The results can then be outside the training region of the data, leading to an imprecise identification of optimality. Alternatively, one may actively identify the true optimality by iteratively exploiting the model (identifying

optimal conditions), conducting experiments, and refining the model using this data. Furthermore, these applications focus on identifying the best conditions in terms of maximizing reactant conversion or H_2 yields. However, since an important goal of plasma catalysis is sustainability, i.e., decarbonization through electrification, we argue that optimal conditions need to be identified in terms of sustainability-based metrics derived from life cycle analysis (LCA) environmental impact calculations. Since syngas product sustainability during bireforming will chiefly depend on the interplay between the environmental impacts of heat generation (to evaporate water to shift the reaction products toward H_2 as well as to heat up the plasma reactor to accelerate the reaction kinetics as well as shift the equilibrium) and electricity use in a plasma reactor, using greenhouse (GHG) emissions as a chief environmental indicator is crucial in evaluating the overall sustainability of the process for the informed optimization. This already suggests a series of optimization constraints since electricity can be sourced not only from the conventional mix that includes coal but also from renewables such as wind or photovoltaics. However, ultimately, a rigorous LCA analysis that also accounts for the consumption of CO_2 feed, the GHG emissions associated with the feed, and the end of life of the syngas reaction product (e.g., methanol or hydrogen) is needed to fully understand the impact of plasma catalysis on overall decarbonization and sustainbility.

In this study, an active optimization approach utilizing the response surface methodology (RSM)[28,29] was applied to improve the performance of plasma-assisted bireforming on the $La_{0.7}Ce_{0.3}NiO_3$ perovskite catalyst. The active optimization process involved the consideration of various input parameters, including the total flow rate, discharge power, CO_2/CH_4 ratio, and steam concentration. Among the notable findings of this study, the energy consumption of conventional dielectric barrier discharge (DBD) technology was assessed, thus providing a valuable benchmark for understanding the energy efficiency improvements achieved by the plasma-assisted bireforming approach. Significant advancements in CH_4 conversion rates were achieved through optimized DBD technology.

The issue of stability within DBD technology was also addressed, with optimal operating conditions being identified that contribute to a longer-lasting and more stable performance, a key aspect of practical viability. The carbon footprint was minimized in terms of kg CO_2 equivalent/kg H_2 yield. Crucially, process-related performance variables, including the H_2 yield, CO yield, and a first-order apparent rate constant (k_{app}), were optimized, thereby facilitating comprehensive comparative analyses. The active optimization process aimed to identify the optimal combination of input parameters that yielded these significant findings, and it involved the iterative updating of the model with additional data points until convergence.

Through this innovative approach, efforts were made to enhance the efficiency, effectiveness, and environmental impact of the plasma-assisted bireforming (BRM) process on the $La_{0.7}Ce_{0.3}NiO_3$ perovskite catalyst.

■ METHODOLOGY

$La_{0.7}Ce_{0.3}NiO_3$ Perovskite Catalyst Synthesis. The nickel-based perovskite catalyst was synthesized by a sol−gel method using $La(NO_3)_3 \cdot 6H_2O$ (99.9%), $Ce(NO_3)_3 \cdot 6H_2O$ (99.5%), and $Ni(NO_3)_2 \cdot 6H_2O$ (98.0%) as precursors and
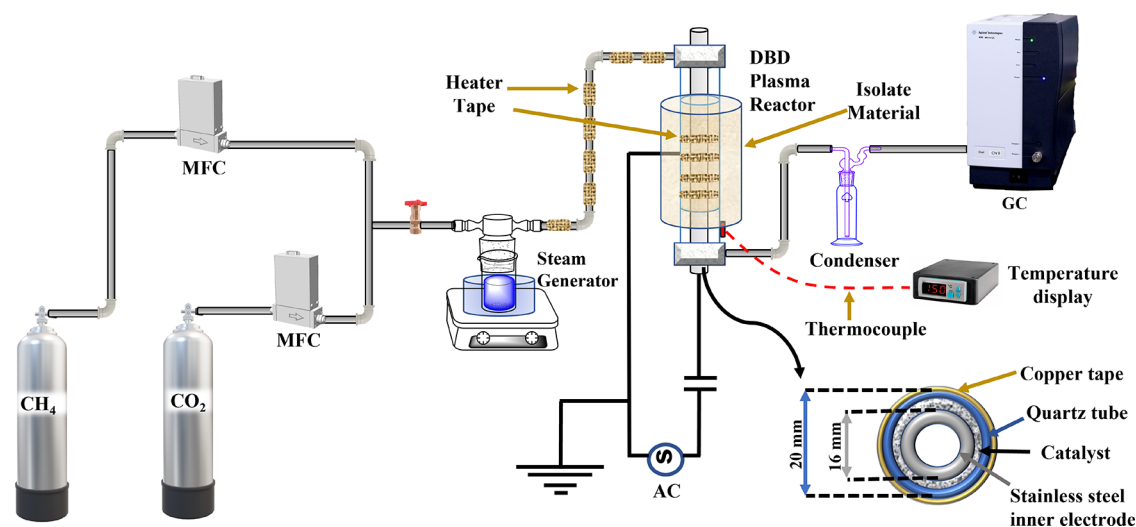
Figure 1. Plasma reactor experimental setup for BRM experiments.

citric acid (99.5%) and ethylene glycol (99.8%) as complexing agents following the methodology proposed by Ranganathan et al.[30] Precursors were purchased from Alfa-Aesar, while complexing agents were used from Sigma-Aldrich. A range of calcination temperatures and reactant compositions were initially explored to arrive at the $La_{0.7}Ce_{0.3}NiO_3$ perovskite catalyst that contained the least secondary phases. For a comprehensive understanding of the process, please refer to the Supporting Information.

Perovskite Catalyst Characterization. *X-ray Diffraction.* The catalyst was characterized using XRD to confirm the perovskite structure by employing an Empyrean, PANalytical B.V. diffractometer. The diffraction patterns were recorded using Cu Kα1,2, with a Cu Kα1 wavelength of 1.541 Å and a Cu Kα2 wavelength of 1.544 Å source (λ = 0.154 nm) in the range of 2θ between 10° and 70° with a step size of 0.0131°.

Transmission Electron Microscopy. The morphology analysis of the perovskite catalyst was performed by using scanning transmission electron microscopy (STEM). The powder catalyst sample was sonicated in acetone and drop-cast onto a Cu lacey carbon film for STEM-EDS analysis. STEM-EDS elemental maps were performed using a Thermo Fisher Talos 200X, a 200 keV high-resolution analytical scanning/transmission electron microscope equipped with a four-quadrant energy dispersive X-ray spectrometer for elemental and compositional mapping.

X-ray Photoelectron Spectroscopy. X-ray photoelectron spectroscopy (XPS) is a surface-sensitive analytical technique that can provide valuable information about the chemical composition and electronic state of elements present on the surface of a material. XPS analysis was performed using a SPECS instrument equipped with a μ-FOCUS 600 X-ray monochromator operating in UHV mode. Al Kα radiation was used with an X-ray beam energy of 1486.7 eV and a power of 100 W. A PHOIBOS 1D-DLD hemispherical analyzer (0.85 eV energy resolution) was used to acquire the spectra. Survey spectra were acquired using pass energy of 100 eV, step size of 1 eV, and dwell time of 100 ms. High-resolution scans were acquired using a pass energy of 20 eV, step size of 0.1 eV, and dwell time of 1 s. Scofield relative sensitivity factors (RSF)[31] were used in quantification together with the instrument-measured transmission function and effective attenuation

length correction (EAL).[32] CasaXPS v2.3.6rev1.0Q was employed for all data processing tasks.[33] No charge calibration was used.

Catalytic Evaluation of $La_{0.7}Ce_{0.3}NiO_3$ Perovskite during Bireforming Reaction. The $La_{0.7}Ce_{0.3}NiO_3$ perovskite catalyst was tested during bireforming using a DBD plasma reactor operating at a minimum of 190 °C and atmospheric pressure, as shown in Figure 1. Here, 200 mg of catalyst was dispersed using quartz wool in the discharge section of the reactor. The reactor was composed of a stainless-steel inner electrode (O.D. = 16 mm) and a glass tube (I.O. = 20 mm) which was covered with copper tape which served as the outer electrode with a length of 140 mm. The electric heater that covered the outer electrode was used to increase the temperature to above 190 °C. Pure CH_4 and CO_2 were used, and their flow rates were controlled using Brooks mass flow controllers. Equation 1, an adapted version from a previous research study,[9] was utilized to estimate the steam content added to the system

$$\frac{Q_{CH_4+CO_2}}{Q_{H_2O}} = \frac{101.325\,kPa - P_{H_2O}}{P_{H_2O}} \tag{1}$$

where $Q_{CH_4+CO_2}$ is total flow rate of CH_4 and CO_2, Q_{H_2O} the steam flow rate, and P_{H_2O} the saturated partial pressure of H_2O at selected temperature. Thus, to obtain a specific percentage of steam in the reactant gas mixture, the table of the saturated partial pressure of water at the selected temperature was utilized. The mixture of CH_4, CO_2, and saturated H_2O vapor was introduced to the DBD plasma reactor with the stream temperature higher than 110 °C using heating tape to avoid any steam condensation. Once a steady-state flow of reactant vapors had been established, plasma was applied with a specific discharge power. To quantify gaseous species conversion, yield, and carbon balance, a micro-gas chromatograph (Agilent 490 Micro GC) equipped with flame ionization and a thermal conductivity detector was employed combined with MolSieve 5A (MS5A) with heated inlet and backflush capability and PLOT Q columns. The temperature of the reaction was measured by a K-type thermocouple located close to the reactor outlet. To ensure the system has established an equilibrium, measurements were taken every 5 min until no
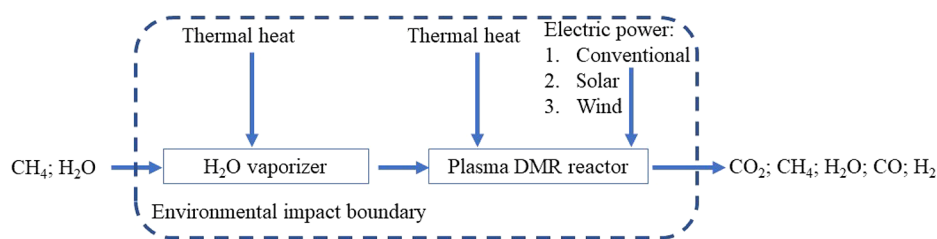
Figure 2. System boundaries (dashed lines) used in the sustainability assessment of the BRM process.

further change in the outlet composition was observed for 3 consecutive measurements.

To calculate the CH_4 and CO_2 conversion, eq 2 was employed

$$x_i\,(\%) = \frac{f_i^{in} - f_i^{out}}{f_i^{in}} \tag{2}$$

To calculate the H_2 and CO flows obtained, eqs 3 and 4 were employed

$$H_2\,(scc/min) = ((GC\ area\ H_2) \times \alpha + \beta) \times f_{Total}^{out} \tag{3}$$

$$CO\,(scc/min) = ((GC\ area\ CO) \times \alpha + \beta) \times f_{total}^{out} \tag{4}$$

The ratio H_2/CO was calculated using eq 5

$$\frac{H_2\,(scc/min)}{CO\,(scc/min)} \tag{5}$$

To calculate the carbon balance, eq 6 was employed

$$B_c\,(\%) = \frac{f_{CH_4}^{out} + f_{CO_2}^{out} + f_{CO}^{out} + f_{C_2H_6}^{out} + f_{C_3H_8}^{out}}{f_{CH_4}^{in} + f_{CO_2}^{in}} \tag{6}$$

where $X_i\,(\%)$ is the conversion of reactant i, $B_c\,(\%)$ the carbon balance of the reaction, $f_i^{in}\,(scc/min)$ the inlet flow of the reactant i, $f_i^{out}\,((GC\ area\ i) \times \alpha + \beta) \times f_{Total}^{out}$, $f_i^{Total}\,(scc/min)$ the flow measured after the outlet condenser, and GC area i the corresponding outlet area of the compound i from the GC (gas chromatograph); α and β are constants obtained from calibration curves for each compound.

The specific energy consumption per flow of hydrogen produced was calculated using eq 7

$$SEI\,(eV/molecule) = \frac{Power\,(W)}{e \times N_A \times f_{Total} \times \frac{P}{RT}} \tag{7}$$

where SEI (eV/molecule) is the specific energy input, and power (W) is the discharge power. $e = 1.602 \times 10^{-19}$ (Joules/eV), $f_{Total}\,(L/s)$ = total flow, N_A = Avogadro's number (6.023×10^{23} molecule/mol), $P = 1$ atm, $T = 293$ K, and $R = 0.08205$ (L × atm)/(mol × °K).

Equation 8 was employed to estimate a pseudo-first-order rate constant for methane consumption

$$k_{app,CH_4}\left(\frac{cm^3}{s \times g}\right) = \frac{v}{w}\left(\ln\left(\frac{1}{1 - X_{CH_4}}\right)\right) \tag{8}$$

where k_{app,CH_4} is the apparent rate constant of CH_4 consumption, v the total volumetric flow (cm^3/s), w the weight of the catalyst (g), and X_{CH_4} the conversion of methane.

Environmental Impact Assessment for Active Process Condition Optimization Calculations. The goal of the environmental assessment performed was to provide quantifiable impacts, here chosen as greenhouse gas emissions resulting from thermal and electrical power inputs. Thermal heat was used for water evaporation for BRM as well as to heat the DBD plasma reactor, while electric power was used for plasma generation. The functional unit was based on 1 kg H_2 produced. Only inputs of electrical and thermal energy and not materials into the process were accounted for in this comparative assessment. Resulting GHG emission scenarios were modeled using SimaPro life cycle assessment software, version 9, using the Ecoinvent version 3 database. Thermal heat supplied from central or small-scale natural gas facilities and medium voltage electricity coming chiefly from the WECC U.S. electric grid subregion were used to represent utility requirements for thermal heat and electric power, respectively. For the green electricity scenario, the DBD reactor was assumed to be fully powered by medium voltage electricity from the WECC U.S. grid region, which was supplied exclusively by 13 MW onshore wind turbines. A second green plasma scenario was used from the WECC U.S. grid region generated by a 570 kWp open-ground photovoltaic multi-Si plant.

The corresponding heat and electric power inputs were calculated during the experiments. First, the thermal heat needed to supply the heat to the DBD plasma reactor in the range from 190 to 450°C, e.g., in thermally assisted plasma catalytic regime, was calculated by measuring the power, in W, of the heating tape used to heat the plasma reactor. The equivalent thermal (nonelectric) heat needed to be supplied, in MJ, was then calculated using eq 9

$$Q_{th_R} = \left(\frac{P_{heater} \times Cap}{Q_{eff}}\right) \times 0.0036 \tag{9}$$

where Q_{th_R} is the thermal heat to the plasma reactor (MJ), P_{heater} the electrical power to the plasma reactor heater (W), Cap the annual capacity of 8000 (h), and Q_{eff} the thermal efficiency of the furnace of 0.6.

Next, electricity for the plasma reactor was calculated using the measured plasma power in W using eq 10

$$P_{pl_R} = \frac{P_{plasma} \times Cap}{1000} \tag{10}$$

where P_{pl_R} is the electricity to the plasma reactor (kWh), P_{plasma} the electrical power to the plasma reactor heater (W), and Cap the annual capacity of 8000 (h).

Finally, thermal heat needed to make process steam was calculated by measuring electrical power in W supplied to the heater/evaporator and converting it to MJ using eq 11

$$Q_{th_{evap}} = \left(\frac{P_{evap} \times Cap}{Q_{eff}} \right) \times 0.0036 \tag{11}$$

where $Q_{th_{evap}}$ is the thermal heat to evaporator (MJ), P_{evap} the electrical power to the evaporator (W), Cap the annual capacity of 8000 (h), and Q_{eff} the thermal efficiency of the furnace of 0.6.

From the values calculated using eqs 9−11 as inputs to the Ecoinvent database, the overall global warming potential was calculated using TRACI method[34] for three different electricity supply scenarios shown in Figure 2, namely, conventional electricity mix, wind electricity, and solar electricity, further in the text referred to as HC, HW, and HS, respectively, in units of kg CO_2 eq/kg H_2.

Notably, the overall values were used in a relative sense for optimization purposes only, since under the experimental design H_2 yields were far from those obtained at high temperatures in a near-equilibrium regime. Therefore, these remain as large upper bounds of the true GWP while they can still be used to compare and contrast the different energy sources. Therefore, while we use these estimates of GWP in our active optimization framework to identify optimal conditions, we do not use these metrics in a quantitative sense.

Active Optimization of Process Conditions. This reaction system is governed by five independent inputs, viz., temperature (X_1), total flow rate (X_2), discharge power of the plasma (X_3), CO_2/CH_4 ratio (X_4), and steam concentration (X_5). Experimental measurements of effluent (the responses) include methane conversion (Y_1), H_2 yield (Y_2), CO yield (Y_3), and first-order apparent reaction rate constant k_{app,CH_4} (Y_4). We actively (iteratively) optimized the inputs (X_i, $i = 1, \cdots, 5$) using a combination of response surface methodology (RSM) and experiments for various process metrics. In particular, we considered seven different metrics for optimization. Four of these metrics directly pertain to direct experimental measurements of the reactants and products, viz., (1) maximizing H_2 yield, (2) maximizing methane conversion, (3) maximizing CO yield, and (4) maximizing apparent rate constant which is calculated by eq 8; three other metrics were considered, namely, minimizing GWP (kg CO_2 eq/kg H_2) assuming the energy input for heating (to modulate temperature) came from traditional sources (i.e., fossil fuel) while the power required for plasma came from (1) conventional source mix including coal and termed HC, (2) solar energy (HS), and (3) wind energy (HW). Fits were better for the logarithm of these three metrics; therefore, the corresponding responses are log(HC) (Y_5), log(HW) (Y_6), and log(HS) (Y_7), which we aimed to minimize. Although the apparent rate constant is dependent on methane conversion, it is further conditioned by flow rate; therefore, the trends in these two metrics will be different.

The complete optimization process is summarized in Figure 3. It can be regarded as an active learning process because we iteratively updated the models based on feedback from experiments conducted at model-predicted optimal conditions.

The detailed explanations for each step in Figure 3 are enclosed in section 1.2 of the Supporting Information (SI). All relevant metrics were optimized simultaneously. All statistical analyses and fitted models generated during the optimization process are included in sections 2−4 of the Supporting Information. Boundaries for input variables at each performed
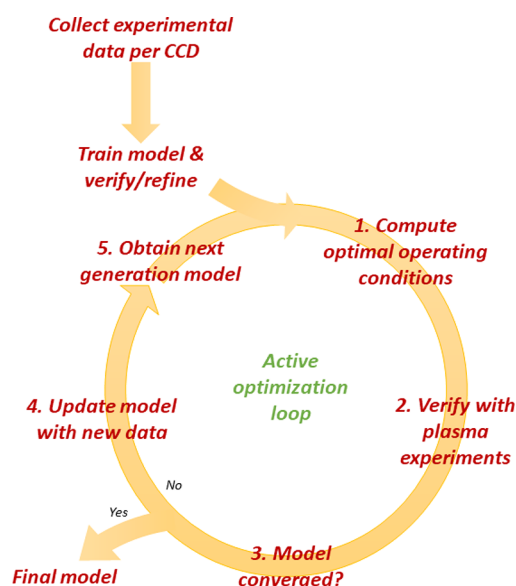

Figure 3. Schematic of the active learning (optimization) workflow that was employed to optimize plasma-catalyzed bireforming.

round of optimization are listed in Table S5, Table S8, and Table S11 in SI.

■ RESULTS AND DISCUSSION

Physicochemical Characterization of La$_{0.7}$Ce$_{0.3}$NiO$_3$ Perovskite Catalyst. Three calcination temperatures (600, 700, and 800 °C) and two different reactant ratios (La$_{0.7}$Ce$_{0.3}$NiO$_3$, and La$_{0.3}$Ce$_{0.7}$NiO$_3$) were explored. Figure 4
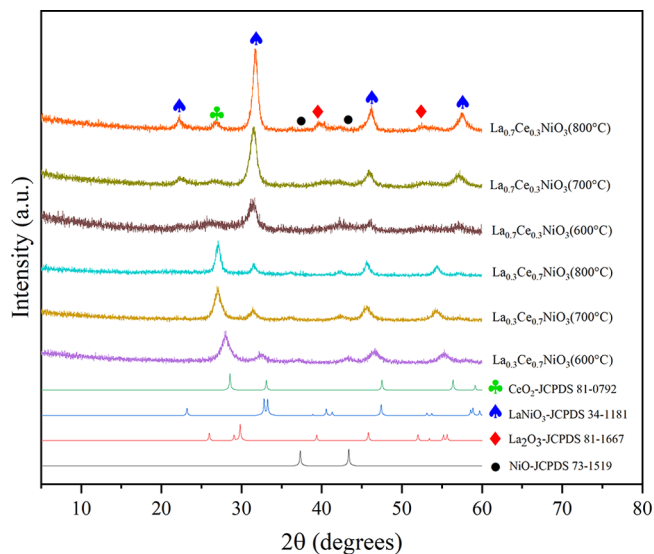
Figure 4. XRD of perovskites calcined at different temperatures.

presents the XRD patterns of the resulting La−Ce−Ni materials. The La$_{0.7}$Ce$_{0.3}$NiO$_3$, upon synthesis, was subjected to temperatures of 600, 700, and 800 °C. Remarkably, at all three temperature levels, the perovskite phase (LaNiO$_3$) was observed to form consistently. Nevertheless, the pattern also exhibited diffraction lines from secondary phases such as the CeO$_2$ and La$_2$O$_3$ phases at higher calcination temperatures. The rhombohedral structure of the LaNiO$_3$ phase was detected according to the peaks at 22.8°, 32.5°, 47.2°, and 58° with

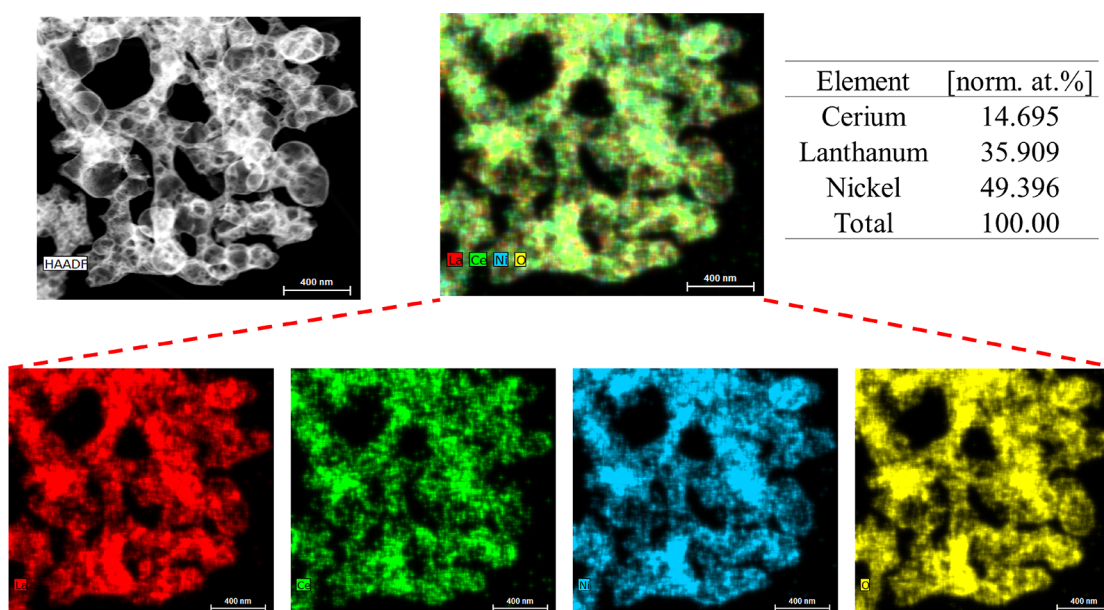| Element	[norm. at.%]
Cerium	14.695
Lanthanum	35.909
Nickel	49.396
Total	100.00

Figure 5. STEM-EDS of $La_{0.7}Ce_{0.3}NiO_3$ calcined at 600 °C.

lattice planes (101), (110), (202), and (122), respectively. These values match the JCPDS no. 34-1028 card.[35] The highest intensity peak observed at 32.5° for all catalysts showed a slight displacement toward a lower 2θ value. This could be attributed to the infiltration of cerium ions, which have a size of 114 pm, into the perovskite lattice and the substitution of some of the La ions, which have a larger size of 136 pm.[36]

In contrast, $La_{0.3}Ce_{0.7}NiO_3$ does not display the same peaks as $La_{0.7}Ce_{0.3}NiO_3$. Some studies[37−39] suggest that a high Ce^{3+} doping content in $La_{1−x}Ce_xNiO_3$ causes certain Ce ions to convert to Ce^{4+} (0.98 pm) and separate from the perovskite phase as CeO_2 as well as facilitate NiO phase segregation. The peak with high intensity at 28.6° was assigned to the (111) lattice plane of the cubic structure of the CeO_2 phase in accordance with the JCPDS no. 81-0792 card.[40] The peaks located at 37.3° and 43.2° were assigned to (112) and (220) lattice planes of the cubic NiO according to JCPDS no. 75-0197card.[41] The small peaks located at 39.18° and 52.3° which are associated with the planes (110) and (024) refer to the hexagonal phase of La_2O_3 according to JCPDS no. 81-1667card.[42] Importantly, according to Silva et al., the $LaNiO_3$ catalyst with a lower cerium content in its structure resulted in higher catalytic activity and reduced carbon formation during hydrogen production from steam reforming of petroleum gas.[41] Further, Rida et al. showed that the catalytic activity of perovskite catalysts synthesized through a sol−gel method and subjected to different calcination temperatures was the highest of the perovskite calcined at 600 °C when compared to the catalyst calcined at 750 °C.[43] Thus, in this research, the $La_{0.7}Ce_{0.3}NiO_3$ catalyst calcined at 600 °C was chosen as the primary catalyst for conducting BRM reactions.

Energy dispersive X-ray spectroscopy (EDS) combined with scanning transmission electron microscopy (STEM) was used to investigate the bulk chemical composition of the $La_{0.7}Ce_{0.3}NiO_3$ catalyst calcined at 600 °C with high spatial resolution. Figure 5 illustrates the spatial distributions of lanthanum, cerium, nickel, and oxygen and a uniform dispersion of these elements. The elemental composition results confirmed the ratio of the $La_{0.7}Ce_{0.3}NiO_3$ catalyst.

The chemical composition and oxidation state of elements present on the surface of $La_{0.7}Ce_{0.3}NiO_3$ calcined at 600 °C were obtained by X-ray photoelectron spectroscopy. A comprehensive discussion of these findings is available in the Supporting Information. The quantification results revealed that the surface composition of the $La_{0.7}Ce_{0.3}NiO_3$ catalyst consists of 12, 49, and 39 atomic percent of Ce, La, and Ni on a metals basis, respectively. Remarkably, this outcome aligns with the composition obtained through an analysis conducted by EDS.

Active Learning: Iteration 1. The results of the first round of active learning are shown in section 2.4 of the SI. We note that the coefficient of determination (R^2) of the initial models varies between 0.79 and 0.91 (see Figure S1), showing that these initial models are adequate for the first round of optimization. The results of initial optimization demonstrate (see Table S6) that the modeling results are qualitatively correct; however, the difference between the predictions and the experiments indicates that a second iteration of the loop is required.

Active Learning: Iterations 2 and 3. The predicted and experimental results of the second iteration are shown in Table 1. Feasible regions in the second round of optimization were enlarged as shown in Table S8 to obtain improved solutions. The detailed analysis of updated models (with 68 data points), including fitted equations, ANOVA table, model diagnostic plots, and contour plots, is in section 3 of the SI.

In a third round (iteration 3), we further retrained the model with new experimental data (at the optimal conditions of iteration 2, to get a total of 77 data points) and recomputed the optimal results. See section 4 in the SI for detailed analysis for retrained models.

To evaluate if a third round of experimental verification is needed, we consider the plots in Figure 6 which compare the predicted and experimental responses in each round (iteration) of active learning (only the predicted values are shown for round 3) for each of the seven metrics. Here, 95% confidence intervals for the predicted values are also presented. It can be seen that the predicted and experimental extrema improve in

Table 1. Second Round Optimal Conditions with Predicted and Experimental Values of Metrics

Metrics	Optimal conditions[a]						Responses[b]						
	X_1	X_2	X_3	X_4	X_5		Y_1	Y_2	Y_3	Y_4	Y_5	Y_6	Y_7
Max CH$_4$	450	101.2	110	4.44	70	Experimental	87.68 ± 0.49	3.11 ± 0.22	12.09 ± 0.33	17.62 ± 0.68	9.12 ± 0.07	8.7 ± 0.07	8.76 ± 0.07
						Predicted	97.09	9.33	11.53	16.09	8.53	7.97	7.96
Max H$_2$	450	200	110	0.5	46.4	Experimental	45.95 ± 2.26	32.47 ± 0.10	23.44 ± 0.87	10.26 ± 0.71	6.75 ± 0.03	6.34 ± 0.03	6.39 ± 0.03
						Predicted	56.95	31.23	24.96	21.43	7.39	6.87	6.83
Max CO	450	200	110	6.02	15.89	Experimental	70.46 ± 1.15	4.61 ± 0.48	27.66 ± 1.82	20.32 ± 0.64	8.62 ± 0.90	8.16 ± 0.90	8.22 ± 0.90
						Predicted	58.07	9.18	38.70	22.44	8.85	8.28	8.26
Max k_{app}	450	200	110	6.08	70	Experimental	81.95 ± 0.56	6.21 ± 0.34	23.77 ± 0.64	28.53 ± 0.52	8.42 ± 0.05	8.01 ± 0.05	8.07 ± 0.05
						Predicted	82.19	7.73	21.53	30.97	8.67	8.19	8.15
Min Log(HC)	379.57	141.14	110	0.5	46.43	Experimental	62.13 ± 2.26	29.77 ± 0.87	21.87 ± 0.82	11.41 ± 0.68	6.84 ± 0.03	6.42 ± 0.03	6.48 ± 0.03
						Predicted	56.80	22.95	15.05	12.14	6.51	5.91	5.93
Min Log(HW)	367.65	139.03	110	0.5	44.84	Experimental	58.62 ± 1.23	28.2 ± 0.11	19.68 ± 0.41	10.22 ± 0.34	6.9 ± 0.01	6.48 ± 0.01	6.53 ± 0.01
						Predicted	54.33	22.11	14.44	11.32	6.51	5.91	5.93
Min Log(HS)	379.36	140.24	110	0.5	45.68	Experimental	61.71 ± 1.03	29.99 ± 0.87	22.03 ± 1.65	11.20 ± 0.31	6.83 ± 0.03	6.41 ± 0.03	6.47 ± 0.03
						Predicted	56.50	22.89	15.09	11.97	6.51	5.91	5.92

[a]X_1: Temperature (°C). X_2: Total flow rate (cm³/min). X_3: Discharge power (W). X_4: CO$_2$/CH$_4$. X_5: Steam concentration (%). [b]Y_1: CH$_4$ conversion (%). Y_2: H$_2$ (cc/min). Y_3: CO (cc/min). Y_4: k_{app,CH_4} (cm³/(s × g)). Y_5: log(HC) (kg CO$_2$ eq/kg H$_2$). Y_6: log(HW) (kg CO$_2$ eq/kg H$_2$). Y_7: log(HS) (kg CO$_2$ eq/kg H$_2$).

the first two rounds for methane conversion, H$_2$ yield, k_{app}, log(HC), log(HW), and log(HS). The experimental CO yield at the predicted optimal point in the second iteration is lower than the measured yield of the first round although it is already close to the lower bound of 95% confidence interval of the prediction. A possible reason for the discrepancy is the extent to which the optimal conditions deviate from the training data and the optimal points identified in the two previous rounds (hence reducing the validity of the model).

Further, the third round of prediction is close to that in the second round for HS, HW, and HC, and the optimal conditions are similar between rounds 2 and 3 (except for temperature). The results of third round optimization are summarized in section 4.4 of the SI. Considering that there is a model-experimental mismatch for all models after each iteration, we posit that the differences between the predicted optimal solutions of rounds 2 and 3 are within these errors. For instance, the differences between the predicted H$_2$ yields in round 3 and experimental yields in round 2 are about 1% or lower for the cases of minimizing log(HC), log(HW), and log(HS), well within the modeling errors of the H$_2$ yield model. In addition, almost all 95% confidence intervals cover the corresponding experimental values in round 2 iteration. Except for optimal CO yield production, the experimental values of other metrics under corresponding optimal conditions are all within 11% of their predicted values in round 2. But the experimental value of predicted optimal CO yield is fairly close to the lower bound of its 95% confidence interval. Therefore, we concluded that we have reached sufficient convergence for the second-order polynomial model we employed and terminated the active learning process after two rounds of experimentation.

The experimental results after round 2 (Table 1) clearly demonstrate how the optimal conditions vary from one metric to the other. Specifically, Table 1 shows that the maximum methane conversion is 88%, the maximum H$_2$ yield is 32.5%, the maximum CO yield is ≈35%, and the highest first-order apparent reaction rate constant is 28.53 cm³/s × g. To maximize these process metrics, our active learning strategy essentially maximized the energy input (temperature and plasma power). Maximizing methane conversion naturally forced the flow rate to be low (in order to increase residence time); however, the active learning ultimately did not require the flow to be at a lower bound. A large CO$_2$/CH$_4$ ratio is required, and steam concentration was pushed to the maximum value of 70% (in both rounds 2 and 3). Maximizing the apparent rate constant is consistent with the methane conversion results except that the methane concentration in the feed is further reduced, and the flow rate is increased to the upper bound. Maximizing the hydrogen yield requires a lower steam concentration (46%) compared to the conditions for maximum methane conversion. Maximizing CO yield requires an even lower steam concentration of ≈16% and a high CO$_2$ concentration in the feed (CO$_2$/CH$_4$ ratio greater than 6) relative to the conditions for maximizing H$_2$ yield (where the CO$_2$/CH$_4$ ratio in the feed is pushed to its minimum). This is because steam reforming (with or without a water gas shift reaction) produces more hydrogen and less CO than dry reforming per mole of methane consumed.

Optimization results based on GWP metrics are closer to the conditions for maximizing hydrogen. Plasma power is maximized for all three cases, while the CO$_2$/CH$_4$ ratio in the feed is reduced to the minimum allowed, indicating that
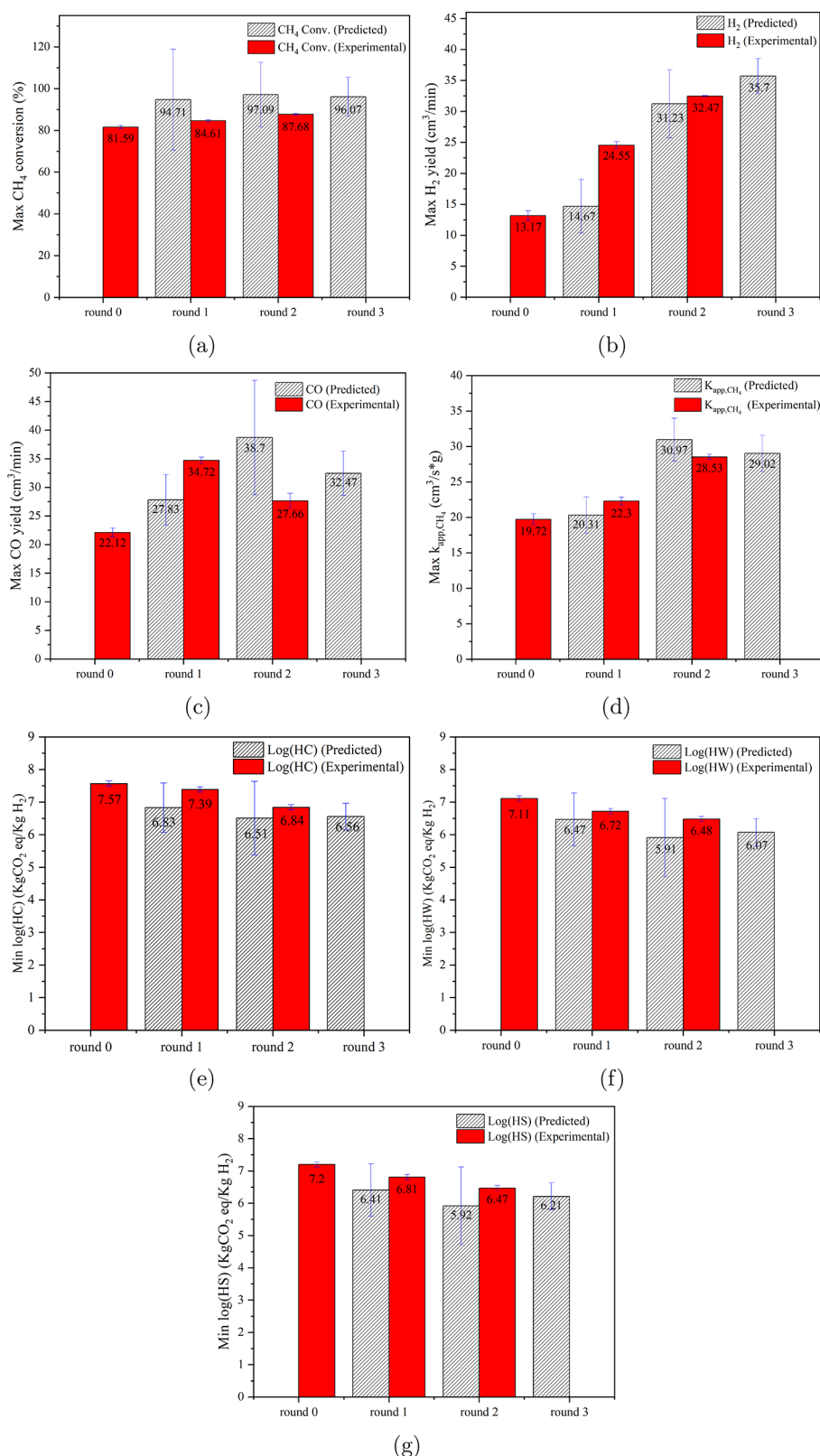
Figure 6. Improvements through active learning (round 0 corresponds to initial experiments): (a) Methane conversion, (b) H_2 yield, (c) CO yield, (d) k_{app,CH_4}, (e) log(HC), (f) log(HW), and (g) log(HS). The error bars of experimental values are generated by the two standard deviation rule and the error bars of predicted values are 95% confidence intervals. They are all shown in blue.

there is a push toward increasing hydrogen production. The flow rates are set to an intermediate value ($\approx$140 cm^3/min), and the steam concentration is about 45%. These settings

result in methane conversion between 60% and 65% and hydrogen yield close to 30% (compared to the experimental maximum of 88% for methane conversion and 32.5% for

Table 2. Catalytic vs Noncatalytic Contributions under Optimal Conditions

Metrics	Optimal conditions[a]						Responses[b]			
	X_1	X_2	X_3	X_4	X_5		P_1	P_2	P_3	P_4
Max CH$_4$	450	101.2	110	4.44	70	Catalyst	87.67 ± 0.48	3.11 ± 0.22	11.75 ± 0.33	16.570
						Noncatalyst	72.26 ± 0.96	1.93 ± 0.04	10.76 ± 0.16	
Max H$_2$	450	200	110	0.5	46.4	Catalyst	48.11 ± 2.26	32.56 ± 0.10	23.44 ± 0.87	8.371
						Noncatalyst	3.00 ± 1.23	0.46 ± 0.05	2.72 ± 0.58	
Max CO	450	200	110	6.02	15.89	Catalyst	70.45 ± 1.16	5.09 ± 0.48	29.48 ± 1.82	8.371
						Noncatalyst	38.75 ± 1.25	3.64 ± 0.73	13.97 ± 1.18	
Max k_{app}	450	200	110	6.08	70	Catalyst	81.94 ± 0.56	6.20 ± 0.34	24.41 ± 0.65	8.371
						Noncatalyst	59.54 ± 0.92	2.50 ± 0.18	13.71 ± 0.81	
Min Log(HC)	379.57	141.14	110	0.5	46.43	Catalyst	62.13 ± 2.27	29.76 ± 0.87	22.68 ± 0.82	11.874
						Noncatalyst	17.43 ± 0.62	4.64 ± 0.28	2.17 ± 0.12	
Min Log(HW)	367.65	139.03	110	0.5	44.84	Catalyst	59.04 ± 1.24	28.30 ± 0.11	19.67 ± 0.42	12.044
						Noncatalyst	10.42 ± 0.21	0.99 ± 0.11	0.70 ± 0.08	
Min Log(HS)	379.36	140.24	110	0.5	45.68	Catalyst	61.71 ± 1.03	29.99 ± 0.88	22.03 ± 1.65	11.958
						Noncatalyst	11.65 ± 1.85	2.96 ± 0.33	0.62 ± 0.08	

[a]X_1: Temperature (°C). X_2: Total flow rate (cm^3/min). X_3: Discharge power (W). X_4: CO$_2$/CH$_4$. X_5: Steam concentration (%). [b]P_1: CH$_4$ conversion (%). P_2: H$_2$ (cc/min). P_3: CO (cc/min). P_4: SEI (eV/molecule).

hydrogen yield). Finally, we note that switching from a coal-based electricity source to a renewable energy source can result in a 30%−35% reduction in GWP under their respective optimal conditions.

Catalytic vs Noncatalytic Contributions. To elucidate the impact of including a catalyst in this system, we ran experiments without the catalyst under the optimal conditions from round 2; the results are shown in Table 2 for the seven metrics. We compute the ratio, γ, of conversion (of methane) or yield (of H$_2$ or CO) without and with the catalyst (i.e., $0 \leq \gamma \leq 1.0$), and plot them versus SEI in Figure 7 for the seven optimal conditions of Tables 1 and 2. The results indicate that the contribution from gas phase reactions is dependent on the reaction conditions and varies from 6% to 82% for methane conversion, 1% to 95% for hydrogen yield, and 3% to 6% for the CO yield. At the conditions that maximize methane conversion (in the presence of a catalyst), nearly 82% of methane reacted is attributable to the gas phase (or that promoted by the packing material). On the other hand, under the condition that maximizes hydrogen yield, 99% of the flux to H$_2$ is due to the catalyst. Under conditions that maximize the CO yield, the contribution of the catalyst is a little less than half (45%). Arguably, this variation in the contribution of the catalyst is dependent on the energy supplied to the system; the higher the specific energy input (SEI) is, the higher the plasma excitation and reactions in the gas phase are. However, the plots in Figure 7 which compare γ_{CH_4}, γ_{H_2}, and γ_{CO} are not consistent with this hypothesis alone. For instance, it can be seen in Figure 7a that a relatively low SEI for the case of maximum hydrogen yield (8.37 eV/molecule) does lead to a higher contribution from the catalyst ($\gamma_{CH_4} = 0.065$) compared to the maximum methane conversion case (where the SEI is 16.57 eV/molecule and $\gamma_{CH_4} = 0.824$). However, for the cases of maximum k_{app} and maximum CO yield, while the SEI is still 8.37 eV/molecule, the catalyst contribution is less than 50% (i.e., $\gamma_{CH_4} > 0.5$), which is much lower than that for the case of maximum hydrogen yield. Furthermore, the conditions for minimizing HC, HW, and HS all have an intermediate SEI value (12 eV/molecule), and the catalyst contribution toward methane consumption is also intermediate at around 70%−
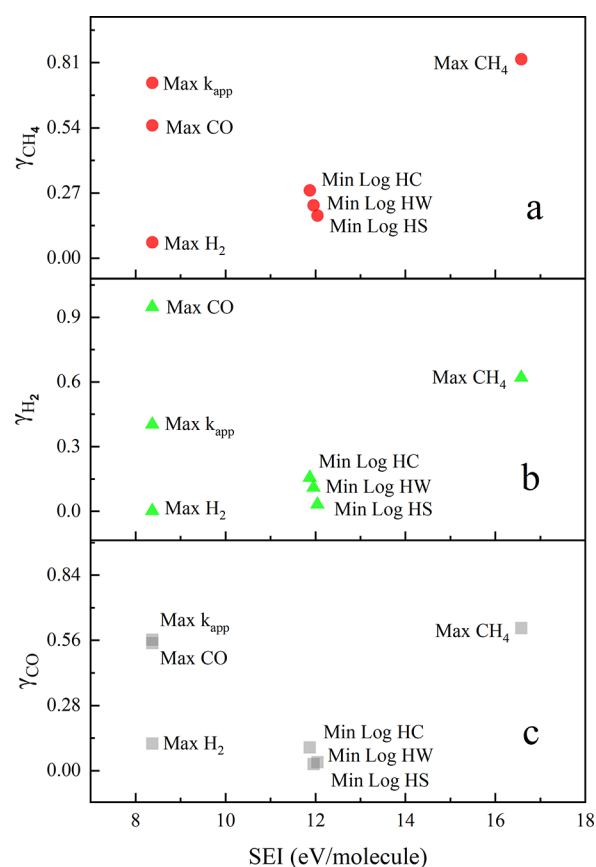

Figure 7. Catalytic vs noncatalytic contributions: (a, b, c) scatter plots of γ_{CH_4} (ratio of methane conversion without and with catalyst), γ_{H_2} (ratio of hydrogen yield without and with catalyst), and γ_{CO} (ratio of CO yield without and with catalyst) versus SEI.

83% ($0.17 \leq \gamma_{CH_4} \leq 0.3$). Similar trends can be observed for CO production, i.e., γ_{CO} (see Figure 7c).

For hydrogen production (Figure 7b), the largest value of γ_{H_2} of 0.947 (i.e., catalyst contribution is only 5%) is for the condition to maximize the CO yield followed by the conditions for maximizing methane conversion and k_{app} (resulting in a
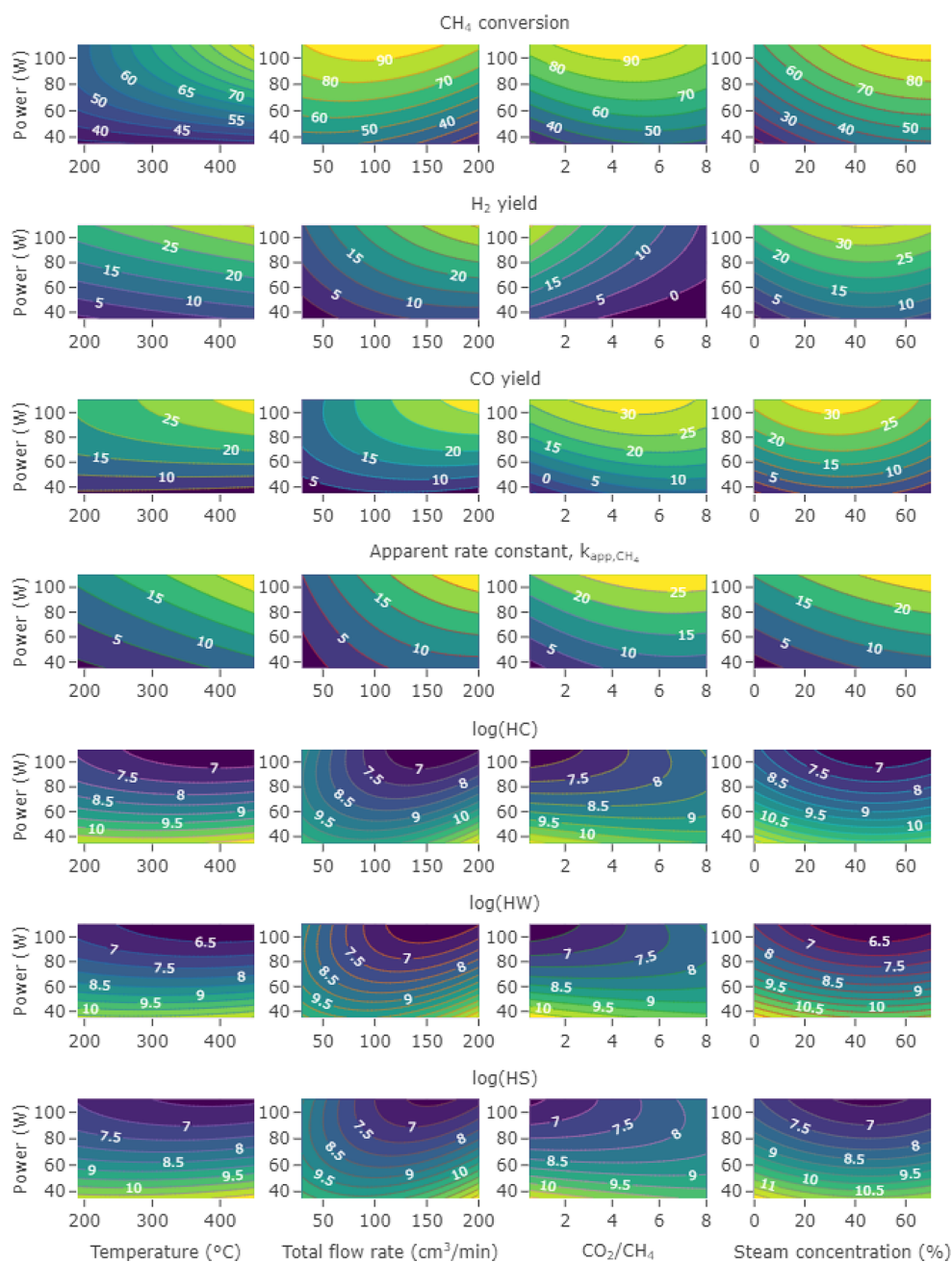
Figure 8. Contour plots of the final models for each metric: Discharge power versus other input variables (temperature, flow rate, CO_2/CH_4 ratio, and steam concentration. The inputs X_i held fixed are at their respective optimum values as shown in Table S13.

small change in relative ordering compared to methane conversion or the CO yield). The highest value of γ_{H_2} (at conditions for maximizing CO yield) occurs when CO_2/CH_4 is ≈ 6 and steam concentration is low ($\approx 15\%$), i.e., under predominantly dry reforming conditions when the concentration of CO_2 is high (and overall hydrogen yield is low even in the presence of the catalyst). On the other hand, under the condition of maximizing the hydrogen yield where a considerably lower CO_2/CH_4 ratio of 0.5 and higher steam concentration (40%) is used, the γ_{H_2} is 0.01; i.e., all of the hydrogen is catalytically generated at these conditions. The conditions to maximize methane conversion and k_{app} both have a high steam concentration (70%), but lead to lower values of γ_{H_2} (varying between 0.4 and 0.6). Since the conditions for

minimizing HC, HS, and HW are close to that for maximum hydrogen yield, the γ_{H_2} values are close but slightly higher (due to higher SEI values in these cases). For methane consumption and CO production (Figures 7a, c), the respective ratios (γ_{CH_4} and γ_{CO}) are also high when the concentration of CO_2 is high (i.e., under conditions that maximize CO yield, methane conversion, or k_{app}); however, a higher steam concentration (corresponding to maximum methane conversion and k_{app}) leads to higher values of γ_{CH_4} and γ_{CO} compared to the conditions for maximum CO yield. To capture these complicated dependencies, multiple linear regression models of the three γ ratios were built with the SEI, CO_2/CH_4 ratio, and steam concentration as three variables to obtain trends in the data. See the details in section 5 of the SI. The analysis

showed that γ values depend positively on the SEI and CO_2/CH_4 ratio in all cases. However, γ_{CO} and γ_{CH_4} values (CO production and methane consumption, respectively) depend positively on steam concentration (although CO production only weakly depends on this variable) while the γ_{H_2} value (for hydrogen yield) is negatively correlated to steam concentration. These observations indicate that the contribution of the catalytic and noncatalytic routes depends on plasma power and process conditions, particularly how "dry" or "wet" the reforming is. Further, they indicate that while catalytic and noncatalytic routes exist for the three plausible reactions in this chemistry (dry reforming, steam reforming, and water gas shift reactions), the dry reforming reaction (which is dominant at high CO_2 and low steam concentration) occurs largely noncatalyzed (or promoted by the packing material), but steam reforming and water gas shift reactions (that occur in the presence of steam) are predominantly catalyzed.

The remarkable activity of the $La_{0.7}Ce_{0.3}NiO_3$ perovskite catalyst to promote the water gas shift reaction could be attributed to the presence of CeO_2, as confirmed by X-ray diffraction (XRD) and X-ray photoelectron spectroscopy (XPS) analyses within the perovskite structure. CeO_2 possesses a unique ability to store and release oxygen, primarily driven by the redox couple between Ce^{4+} and Ce^{3+}. This redox chemistry serves as an oxygen buffer, facilitating the reoxidation of carbon species present on the catalyst surface.[38,39,41] This reoxidation process aids in the efficient removal of coke deposits, ultimately leading to the production of carbon monoxide (CO). Subsequently, CO can react with steam to generate CO_2 and H_2.

Contour Analysis. Figure 8 shows contour plots to understand the effect of discharge power and the other four input variables on each of the seven responses based on the final models (i.e., the retrained models after round 2 experiments and the ones used to generate the results in Table S12). Three inputs are held in each plot at their respective optimal values. Many of the optimal solutions still lie at the bounds; however, the contour plots underline the nonlinear relationship between inputs and responses. We can make several observations:

1. Maximizing temperature and plasma power does lead to increased methane conversion, hydrogen yield, and lower HC, HW, and HS; however, temperature is a relatively less sensitive metric compared to plasma power in this regime (plots in the first column of Figure 8).

2. In this system, the total flow rate determines the residence time as the catalyst amount is kept fixed across experiments. At a given plasma power, for example 100 W, decreasing the flow rate from the maximum increases conversion likely because of a higher residence time for methane. However, a further reduction in the flow rate decreases methane conversion (first plot of the second column of Figure 8). At lower flow rates, the SEI is high implying a higher contribution from noncatalytic pathways which we posit are slower than catalytic routes, thereby leading to a reduction in methane conversion.

3. A high flow rate (second column of plots in Figure 8) maximizes H_2 yield and CO yield metrics, indicating possibly that at lower flow rates (high SEI leading to more gas phase reactions), byproducts such as coke or

larger oxygenates can form, consistent with Figure 7c and the low carbon balance. High flow rates also increase k_{app} which is expected as first-order rate constants are higher at lower conversion (residence times).

4. For log(HC), log(HW), and log(HS), the optimal points have an intermediate value of total flow rate (last three plots of the second column in Figure 8). We posit that this is because the increase in hydrogen yield at intermediate to higher total flow rates is not proportional to the increase in the heat requirements to generate additional process steam (with results in a larger CO_2 footprint).

5. The dependence of the metrics on the CO_2/CH_4 ratio is quite complicated. For methane conversion, a low CO_2/CH_4 ratio results in less dry reforming (consequently a lower methane conversion). However, a higher ratio also seemingly reduces methane conversion, but this could be an artifact of the quadratic models used as training data largely have a CO_2/CH_4 ratio less than 6. Increasing the CO_2/CH_4 ratio decreases hydrogen yield, as methane concentration in the feed is lowered. Increasing the CO_2/CH_4 ratio initially increases CO yield; at a CO_2/CH_4 ratio greater than 6, the yield is shown to drop which could also be due to model artifacts. k_{app} increases with the CO_2/CH_4 ratio possibly indicating a higher order dependence of CO_2 on dry reforming. The GWP-based metrics are at their lowest at the minimum value of the CO_2/CH_4 ratio, tracking the behavior of the H_2 yield plot. Arguably, including the consumption of CO_2 into a more full-fledged sustainability metric might push the optimality to a higher CO_2/CH_4 ratio.

6. A higher steam concentration increases methane conversion and k_{app}, possibly because methane concentration is lowered and potentially points to a positive order dependence of water vapor on reforming kinetics.

7. The dependence of H_2 yield on steam is more complicated. At lower steam concentrations, hydrogen yield increases with increasing steam inflow as it results in increased steam reforming. However, at higher steam concentrations, any increase in steam inflow decreases methane concentration which, in turn, decreases hydrogen availability in the feed and thereby reduces hydrogen yield.

8. At low steam concentrations, CO yield increases with increasing steam inflow, possibly because CO is a potential product of steam reforming; at higher steam concentrations, however, increasing steam inflow decreases the amount of carbon influx as well as promotes the water gas shift reaction to push CO to CO_2.

9. The dependence of HC, HW, and HS on steam concentration tracks the H_2 yield plot.

■ CONCLUSIONS

The $La_{0.7}Ce_{0.3}NiO_3$ perovskite catalyst was successfully synthesized by a three-step sol−gel method. Furthermore, the utilization of a $La_{0.7}Ce_{0.3}NiO_3$ perovskite catalyst in a dielectric barrier discharge (DBD) plasma bireforming process at mild conditions has demonstrated remarkable activity to produce syngas. Through the implementation of a central composite design (CCD) experiment coupled with an active

learning optimization process, we have identified optimal conditions for minimizing the carbon footprint and maximizing other key performance indicators such as CH_4 conversion, CO_2 conversion, H_2 yield, CO, and first-order apparent reaction rate constant (k_{app}) in the DBD plasma bireforming process. The optimal process conditions are heavily dependent on the metrics (key indicators) to be optimized. Dry reforming, steam reforming, and water gas shift reactions all have noncatalytic (purely driven by plasma) and catalytic (driven synergistically by plasma and catalyst) routes; dry reforming appears to be predominantly noncatalytic while steam reforming and water gas shift reactions are predominantly catalytic. Minimizing global warming potential, in terms of inferred CO_2 footprint normalized to hydrogen throughput, results in maximizing hydrogen yield through steam reforming (and water gas shift reactions) at an SEI of ≈12 eV/molecule.

The successful integration of the $La_{0.7}Ce_{0.3}NiO_3$ perovskite catalyst and the optimization process using a CCD experiment coupled with an active learning optimization process has demonstrated the power of combining advanced materials and experimental design techniques. This synergy opens up new avenues for improving and tailoring the performance of plasma-based processes, paving the way for more sustainable and efficient energy conversion technologies.

■ ASSOCIATED CONTENT

ⓢ Supporting Information

The Supporting Information is available free of charge at https://pubs.acs.org/doi/10.1021/acssuschemeng.3c06929.

> Details on the experimental design and RSM, compiled final experimental data with the independent variables and responses, initial models for all seven responses, model diagnostics, and detailed optimization results for all optimization rounds (PDF)

■ AUTHOR INFORMATION

Corresponding Authors

Wei-Min Huang − *Department of Mathematics, Lehigh University, Bethlehem, Pennsylvania 18015, United States*; Email: wh02@lehigh.edu

Srinivas Rangarajan − *Department of Chemical and Biomolecular Engineering, Lehigh University, Bethlehem, Pennsylvania 18015, United States*; ⓞ orcid.org/0000-0002-6777-9421; Email: srr516@lehigh.edu

Jonas Baltrusaitis − *Department of Chemical and Biomolecular Engineering, Lehigh University, Bethlehem, Pennsylvania 18015, United States*; ⓞ orcid.org/0000-0001-5634-955X; Phone: +1-610-758-6836; Email: job314@lehigh.edu

Authors

Diego Alexander Gonzalez-Casamachin − *Department of Chemical and Biomolecular Engineering, Lehigh University, Bethlehem, Pennsylvania 18015, United States*

Tian Qin − *Department of Mathematics, Lehigh University, Bethlehem, Pennsylvania 18015, United States*

Lihua Zhang − *Brookhaven National Laboratory Center for Functional Nanomaterials, Upton, New York 11973-5000, United States*

Complete contact information is available at:
https://pubs.acs.org/10.1021/acssuschemeng.3c06929

Author Contributions

‖Diego Alexander Gonzalez-Casamachin and Tian Qin contributed equally.

Notes

The authors declare no competing financial interest.

■ ACKNOWLEDGMENTS

■ REFERENCES

(1) Mallapragada, D. S.; et al. Decarbonization of the chemical industry through electrification: Barriers and opportunities. *Joule* **2023**, *7*, 23−41.

(2) Dincer, I.; Acar, C. Review and evaluation of hydrogen production methods for better sustainability. *Int. J. Hydrogen Energy* **2015**, *40*, 11094−11111.

(3) Zhu, X.; Liu, X.; Lian, H.-Y.; Liu, J.-L.; Li, X.-S. Plasma catalytic steam methane reforming for distributed hydrogen production. *Catal. Today* **2019**, *337*, 69−75.

(4) Cho, H. H.; Strezov, V.; Evans, T. J. Environmental impact assessment of hydrogen production via steam methane reforming based on emissions data. *Energy Reports* **2022**, *8*, 13585−13595.

(5) Simpson, A. P.; Lutz, A. E. Exergy analysis of hydrogen production via steam methane reforming. *Int. J. Hydrogen Energy* **2007**, *32*, 4811−4820.

(6) Wismann, S. T.; Engbæk, J. S.; Vendelbo, S. B.; Bendixen, F. B.; Eriksen, W. L.; Aasberg-Petersen, K.; Frandsen, C.; Chorkendorff, I.; Mortensen, P. M. Electrified methane reforming: A compact approach to greener industrial hydrogen production. *Science* **2019**, *364*, 756−759.

(7) Wismann, S. T.; Engbæk, J. S.; Vendelbo, S. B.; Eriksen, W. L.; Frandsen, C.; Mortensen, P. M.; Chorkendorff, I. Electrified methane reforming: Elucidating transient phenomena. *Chemical Engineering Journal* **2021**, *425*, 131509.

(8) Wismann, S. T.; Engbæk, J. S.; Vendelbo, S. B.; Eriksen, W. L.; Frandsen, C.; Mortensen, P. M.; Chorkendorff, I. Electrified Methane Reforming: Understanding the Dynamic Interplay. *Ind. Eng. Chem. Res.* **2019**, *58*, 23380−23388.

(9) Cao, G.; Xiao, Y.; Huang, W. M.; Chen, C. H.; Baltrusaitis, J. DBD plasma-assisted ethanol steam reforming for green H_2 production: Process optimization through response surface methodology (RSM). *Int. J. Hydrogen Energy* **2023**, *48*, 553−565.

(10) Nozaki, T.; Tsukijihara, H.; Fukui, W.; Okazaki, K. Kinetic Analysis of the Catalyst and Nonthermal Plasma Hybrid Reaction for Methane Steam Reforming. *Energy Fuels* **2007**, *21*, 2525−2530.

(11) Tu, X.; Whitehead, J. Plasma-catalytic dry reforming of methane in an atmospheric dielectric barrier discharge: Understanding the synergistic effect at low temperature. *Applied Catalysis B: Environmental* **2012**, *125*, 439−448.

(12) Wang, Q.; Shi, H.; Yan, B.; Jin, Y.; Cheng, Y. Steam enhanced carbon dioxide reforming of methane in DBD plasma reactor. *Int. J. Hydrogen Energy* **2011**, *36*, 8301−8306.

(13) Demidov, D. V.; Mishin, I. V.; Mikhailov, M. N. Gibbs free energy minimization as a way to optimize the combined steam and carbon dioxide reforming of methane. *Int. J. Hydrogen Energy* **2011**, *36*, 5941−5950.

(14) King, B.; Patel, D.; Zhu Chen, J.; Drapanauskaite, D.; Handler, R.; Nozaki, T.; Baltrusaitis, J. Comprehensive process and environmental impact analysis of integrated DBD plasma steam methane reforming. *Fuel* **2021**, *304*, 121328.

(15) Goujard, V.; Tatibouët, J. M.; Batiot-Dupeyrat, C. Use of a non-thermal plasma for the production of synthesis gas from biogas. *Applied Catalysis A: General* 2009, 353, 228−235.

(16) Pornmai, K.; Arthiwet, N.; Rueangjitt, N.; Sekiguchi, H.; Chavadej, S. Synthesis gas production by combined reforming of CO_2-containing natural gas with steam and partial oxidation in a multistage gliding arc discharge system. *Ind. Eng. Chem. Res.* 2014, 53, 11891−11900.

(17) Kahle, L. C.; Roussière, T.; Maier, L.; Herrera Delgado, K.; Wasserschaff, G.; Schunk, S. A.; Deutschmann, O. Methane dry reforming at high temperature and elevated pressure: Impact of gas-phase reactions. *Ind. Eng. Chem. Res.* 2013, 52, 11920−11930.

(18) Kumar, N.; Shojaee, M.; Spivey, J. Catalytic bi-reforming of methane: from greenhouse gases to syngas. *Current Opinion in Chemical Engineering* 2015, 9, 8−15.

(19) Liu, F.; Zhao, L.; Wang, H.; Bai, X.; Liu, Y. Study on the preparation of Ni-La-Ce oxide catalyst for steam reforming of ethanol. *Int. J. Hydrogen Energy* 2014, 39, 10454−10466.

(20) Gilbart, B.; Dickenson, A.; Walsh, J. L.; Hasan, M. I. Dominant heating mechanisms in a surface barrier discharge. *J. Phys. D: Appl. Phys.* 2021, 54, 175202.

(21) Sheng, Z.; Watanabe, Y.; Kim, H.-H.; Yao, S.; Nozaki, T. Plasma-enabled mode-selective activation of CH_4 for dry reforming: First touch on the kinetic analysis. *Chemical Engineering Journal* 2020, 399, 125751.

(22) Yu, X.; Dang, X.; Li, S.; Meng, X.; Hou, H.; Wang, P.; Wang, Q. Abatement of chlorobenzene by plasma catalysis: Parameters optimization through response surface methodology (RSM), degradation mechanism and PCDD/Fs formation. *Chemosphere* 2022, 298, 134274.

(23) Ayodele, B. V.; Abdullah, S. An Overview of Response Surface Methodology Approach to Optimization of Hydrogen and Syngas Production by Catalytic Reforming of Greenhouse Gases (CH_4 and CO_2). In *Statistical Approaches with Emphasis on Design of Experiments Applied to Chemical Processes*; Silve, V., Ed.; InTech Open, 2018. DOI: 10.5772/intechopen.73001

(24) Mei, D. H.; Liu, S. Y.; Tu, X. CO_2 reforming with methane for syngas production using a dielectric barrier discharge plasma coupled with Ni/γ-Al_2O_3 catalysts: Process optimization through response surface methodology. *Journal of CO2 Utilization* 2017, 21, 314−326.

(25) Khoja, A. H.; Tahir, M.; Saidina Amin, N. A. Process optimization of DBD plasma dry reforming of methane over Ni/$La_2O_3MgAl_2O_4$ using multiple response surface methodology. *Int. J. Hydrogen Energy* 2019, 44, 11774−11787.

(26) Liu, J.; Zhu, X.; Zhou, C.; Du, J.; Gan, Y.; Chen, G.; Tu, X. Plasma-catalytic ammonia synthesis over $BaTiO_3$ supported metal catalysts: Process optimization using response surface methodology. *Vacuum* 2022, 203, 111205.

(27) Mansouri, F.; Khavanin, A.; Jafari, A. J.; Asilian, H.; Ghomi, H. R.; Mousavi, S. M. Energy efficiency improvement in nitric oxide reduction by packed DBD plasma: optimization and modeling using response surface methodology(RSM). *Environmental Science and Pollution Research* 2020, 27, 16100−16109.

(28) Khuri, A. I. Introduction to Linear Regression Analysis, Fifth Edition by Douglas C. Montgomery, Elizabeth A. Peck, G. Geoffrey Vining. *International Statistical Review* 2013, 81, 318−319.

(29) Raymond, R. H.; Montgomery, D. C.; Anderson-Cook, C. M. *Response Surface Methodology: Process and Product Optimization Using Designed Experiments*, 3rd ed.; John Wiley & Sons, Inc.: Hoboken, NJ, 2009.

(30) Ranganathan, R. V.; Jony, B.; Fondriest, S. M.; Liu, Z.; Wang, R.; Uddi, M. Plasma-catalysis chemical looping CH_4 reforming with water splitting using ceria supported Ni based La-perovskite nano-catalyst. *Journal of CO2 Utilization* 2019, 32, 11−20.

(31) Scofield, J. Hartree-Slater subshell photoionization cross-sections at 1254 and 1487 eV. *J. Electron Spectrosc. Relat. Phenom.* 1976, 8, 129−137.

(32) Seah, M. P. Simple universal curve for the energy-dependent electron attenuation length for all materials. *Surf. Interface Anal.* 2012, 44, 1353−1359.

(33) Fairley, N.; Fernandez, V.; Richard-Plouet, M.; Guillot-Deudon, C.; Walton, J.; Smith, E.; Flahaut, D.; Greiner, M.; Biesinger, M.; Tougaard, S.; Morgan, D.; Baltrusaitis, J. Systematic and collaborative approach to problem solving using X-ray photoelectron spectroscopy. *Applied Surface Science Advances* 2021, 5, 100112.

(34) Bare, J. TRACI 2.0: the tool for the reduction and assessment of chemical and other environmental impacts 2.0. *Clean Technologies and Environmental Policy* 2011, 13, 687−696.

(35) Ribeiro, J. F. S.; Souza, A. A.; Lima, E. C. N. L.; Souza, M. J. B.; Garrido Pedrosa, A. M. Effect of synthesis method of $LaNiO_3$ type materials with perovskite structure on their features and in the methylene blue dye removal from aqueous media. *Scientia Plena* 2021, 16, 1−14.

(36) Yang, E. H.; Kim, N. Y.; Noh, Y. S.; Lim, S. S.; Jung, J. S.; Lee, J. S.; Hong, G. H.; Moon, D. J. Steam CO_2 reforming of methane over $La_{1−x}Ce_xNiO_3$ perovskite catalysts. *Int. J. Hydrogen Energy* 2015, 40, 11831−11839.

(37) Lima, S. M.; Assaf, J. M.; Peña, M. A.; Fierro, J. L. Structural features of $La_{1−x}Ce_xNiO_3$ mixed oxides and performance for the dry reforming of methane. *Applied Catalysis A: General* 2006, 311, 94−104.

(38) Franchini, C. A.; Aranzaez, W.; Duarte de Farias, A. M.; Pecchi, G.; Fraga, M. A. Ce-substituted $LaNiO_3$ mixed oxides as catalyst precursors for glycerol steam reforming. *Applied Catalysis B: Environmental* 2014, 147, 193−202.

(39) Ghafoor, A.; Bibi, I.; Majid, F.; Kamal, S.; Ata, S.; Nazar, N.; Iqbal, M.; Raza, M. A.; Almoneef, M. M. Ce and Fe doped $LaNiO_3$ synthesized by micro-emulsion route: Effect of doping on visible light absorption for photocatalytic application. *Materials Research Express* 2021, 8, 085009.

(40) Sayyed, S. A. A. R.; Beedri, N. I.; Kadam, V. S.; Pathan, H. M. Rose bengal-sensitized nanocrystalline ceria photoanode for dye-sensitized solar cell application. *Bulletin of Materials Science* 2016, 39, 1381−1387.

(41) Silva, P. P.; Ferreira, R. A.; Noronha, F. B.; Hori, C. E. Hydrogen production from steam and oxidative steam reforming of liquefied petroleum gas over cerium and strontium doped LaNiO3 catalysts. *Catal. Today* 2017, 289, 211−221.

(42) Mariscal-Becerraa, L.; Carmona-Téllez, S.; Vázquez-Arreguín, R.; García-Rosas, C. M.; Falcony, C.; Murrieta, H.; Sánchez-Alejob, M. A. Green light emission in aluminum oxide powders doped with different terbium concentrations. *Revista Mexicana de Fisica* 2016, 62, 285−289.

(43) Rida, K.; Pena, M. A.; Sastre, E.; Martinez-Arias, A. Effect of calcination temperature on structural properties and catalytic activity in oxidation reactions of $LaNiO_3$ perovskite prepared by Pechini method. *Journal of Rare Earths* 2012, 30, 210−216.